



# A Remote Sensing–based Intensity–Duration Curve, Faifa Mountains, Saudi Arabia

Sita Karki<sup>1</sup>, Mohamed Sultan<sup>1</sup>, Saleh A. Al-Sefry<sup>2</sup>, Hassan M. Alharbi<sup>2</sup>, Mustafa Kemal Emil<sup>1</sup>, Racha Elkadiri<sup>3</sup>, and Emad Abu Alfadail<sup>2</sup>

5 <sup>1</sup> Department of Geological and Environmental Sciences, Western Michigan University, Kalamazoo, MI USA

<sup>2</sup> Saudi Geological Survey, Jeddah, Kingdom of Saudi Arabia

<sup>3</sup> Department of Geosciences, Middle Tennessee State University, Murfreesboro TN USA

*Correspondence to:* Mohamed Sultan ([mohamed.sultan@wmich.edu](mailto:mohamed.sultan@wmich.edu))

**Abstract.** Construction of intensity-duration (ID) curves and early warning systems for landslides (EWSL) are hampered by  
10 the paucity of temporal and spatial archival data. We developed methodologies that could be used for the construction of an  
ID curve that could be used for the construction of an EWSL over the Faifa Mountains in the Red Sea Hills. The developed  
methodologies relies on temporal, readily available, archival Google Earth and Sentinel-1 imagery, precipitation  
measurements, and limited field data. These methodologies accurately distinguished landslide-producing storms from non-  
landslide producing ones and identified the locations of these landslides with an accuracy of 60%.

## 15 1 Introduction

Mountainous areas worldwide with steep slopes, high precipitation, and limited vegetative cover often experience landslides.  
Two main types of landslides are often reported from Faifa Mountains in Saudi Arabia. The first are debris flows that occur  
when water-saturated soils (largely from weathered bedrock and fragmented rock) move down mountainsides, get channelled  
into streams, pick up objects along their paths, and deposit their thick load down the valley slopes (Iverson, 1997). The second  
20 results from failure along preexisting fracture planes (Lowell, 1990) that occurs when the following conditions are met (Norrish  
and Wyllie, 1996): (1) the strike of the planer discontinuity is similar (within 20°) to the strike of the slope face, (2) the dip of  
the planer discontinuity is less than that of the slope face and oriented in the same general direction, (3) the dip of the planer  
discontinuity is greater than the angle of the friction of the surface, and (4) the friction angle of the rock material is partially  
controlled by the size and shape of the grains exposed on the fracture surface and by the mass of the block above the planer  
25 discontinuity (Alharbi et al., 2014). These two types of landslides pose a substantial threat to human life and property in  
mountainous areas, especially in populated regions that are witnessing unplanned urbanization.

One such area is the Faifa Mountains (area: 119 km<sup>2</sup>) in the Jazan Province of Saudi Arabia (Fig. 1). The population density  
in Faifa is high (~35,000 inhabitants in 137 km<sup>2</sup>; MMRA, 2017), receives relatively high precipitation (mean annual  
30 precipitation [MAP]: 252 mm/year; Fig. 2) compared to the remaining parts of Saudi Arabia (83 mm), has steep slopes (up to  
65°), and witnesses frequent landslide occurrences (1–4 events/year during the study period [2007 to 2017]; Fig. 3).



Unfortunately, monitoring programs for landslide occurrences (date and time) and conditions (intensity and duration of precipitation) are very limited in Faifa. If such programs existed, they would have generated the archival landslide data needed for the construction of intensity-duration (ID) relationships and for the development of an early warning system for landslides (EWSL). The paucity of such data in Faifa is largely caused by its rugged nature and its limited road network coverage; both factors rendered many areas inaccessible and hindered the development of monitoring systems. Despite the absence of organized monitoring programs for landslides in the study area, a few were recorded by the Saudi Geological Survey (SGS) in the past few years. Our field observations and those collected by the SGS revealed that debris flows are **by far the most prominent (>85%) landslide type in the study area.**

To compensate for the deficiencies in field data in Faifa, we complemented the available field data with observations extracted from readily available temporal remote sensing data. These include high-resolution Google Earth images (spatial resolution: 15 m to 15 cm), Sentinel-1A Ground Range Detected (GRD Level-1 radar data; spatial resolution: 10 m), satellite-based precipitation data including Tropical Rainfall Measuring Mission (TRMM, 3-hourly\_3B42 v7, spatial resolution: **0.25°x 0.25°**) and Global Precipitation Measurement (GPM) IMERG Final Precipitation L3 Half Hourly (spatial resolution: 0.1° x 0.1° V05), and a high-resolution digital elevation model (TanDEM-X DEM; spatial resolution: 12 m). Field observations were collected (period: 2014 to 2016) from the areas that witnessed landslides following precipitation events. In this manuscript, we develop procedures that take advantage of readily available remotely acquired data, and limited field data, to develop ID curves for the study area, procedures that could potentially be applied to similar areas with limited field data. The proposed procedures for the development of ID curves should not be considered as alternatives to the well-developed field-based ID relationships and to recently introduced advances in such applications, but could be used in absence of such field-based datasets. These advances include the development of ID relationships that account for the role of antecedent rainfall preceding the landslide-causing precipitation (e.g., Kim et al., 2014, Hong et al., 2017).

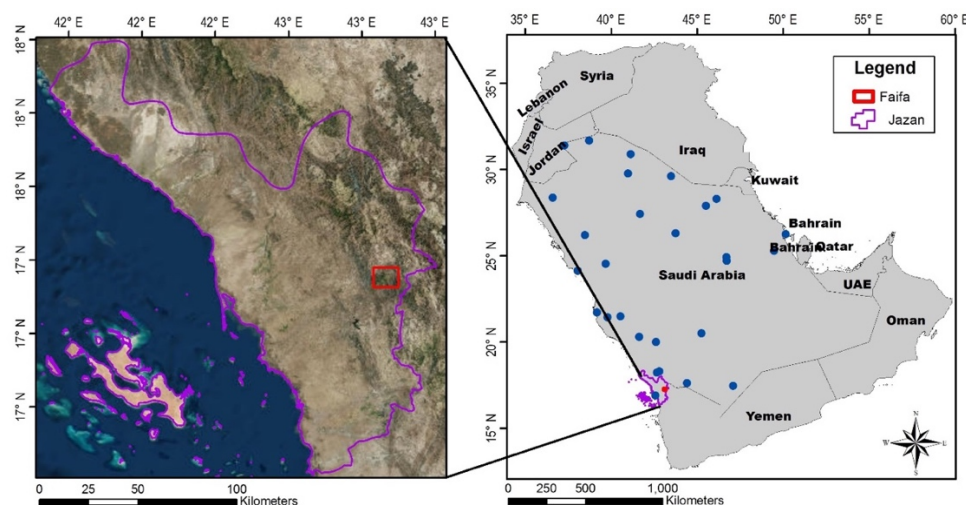


**Figure 1. Location of the Faifa Mountains (outlined by red box) within the Jazan province (outlined by purple polygon). The blue dots represent meteorological stations (Mashat and Basset, 2011) in Saudi Arabia.**

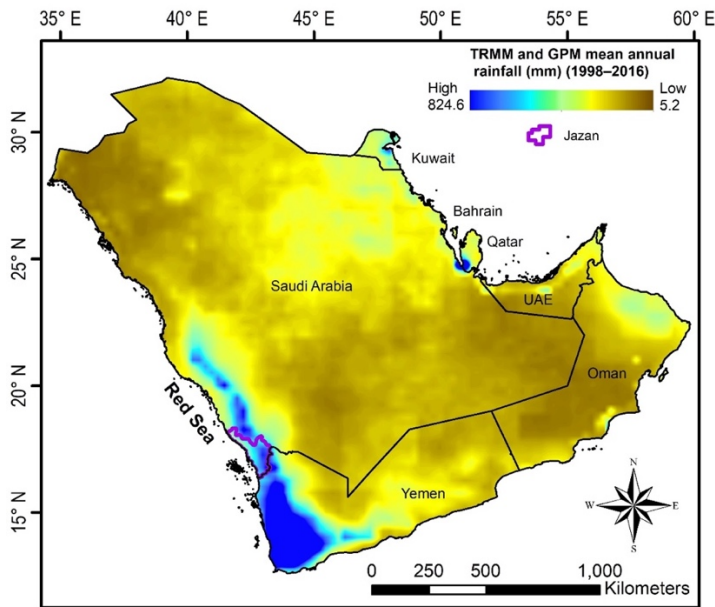
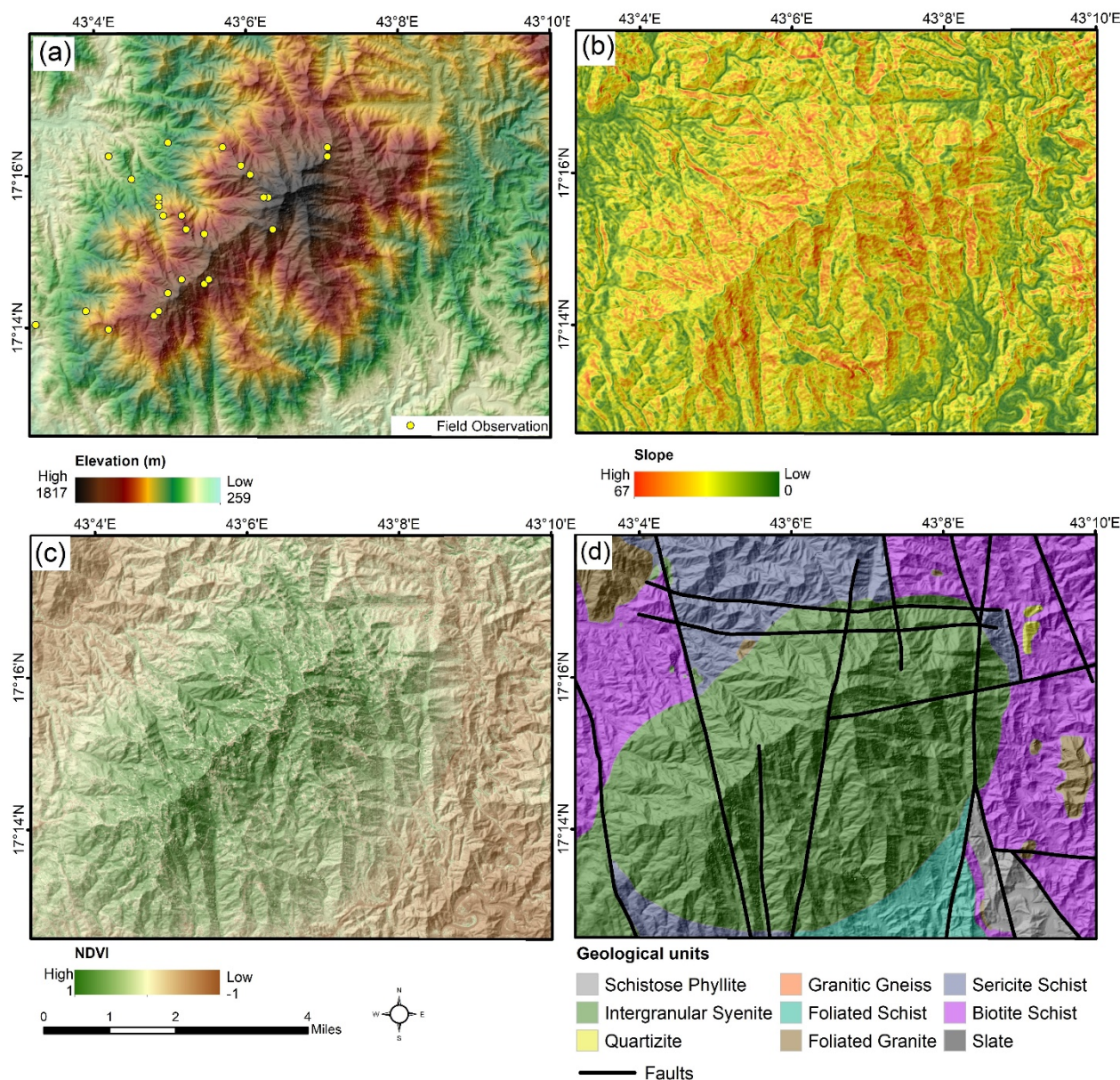


Figure 2. Mean annual precipitation (MAP; 1998–2016) extracted from the combination of TRMM (3-hourly\_3B42 v7, spatial resolution:  $0.25^\circ \times 0.25^\circ$ ) and GPM (IMERG Final Precipitation L3 Half Hourly, spatial resolution:  $0.1^\circ \times 0.1^\circ$  V05) showing the highest regional rainfall in the southeast corner of the Arabian Peninsula including the Jazan Province and Faifa Mountains (MAP in Faifa: 252 mm/year).

### 1.1 Geologic, topographic, and climatic setting of the Faifa Mountains

The study area (119 km<sup>2</sup>) lies within the Red Sea Hills, and covers an area (17.20° N to 17.29° N and from 43.05° E to 43.16° E) proximal to the Saudi-Yemeni border (Fig. 1). The elevation is high (range: 259 to 1817 meters above mean sea level [m.a.m.s.l]) compared to the surrounding lowlands, the topography is steep (slope as high as 67°; Figs. 3a and 3b), and vegetation is extensive over the mountains but sparse in the surrounding lowlands, as shown in the normalized difference vegetation index (NDVI) map (Fig. 3c). The Faifa region is located within the north to northeast trending Tayyah tectonic belt that consists of a complex of metamorphosed volcanic and pyroclastic rocks of basaltic, andesitic, and clastic metasedimentary rocks (Greenwood et al., 1983) that were generated and accreted in an island arc setting some 800 to 900 Ma (Stoeser and Camp, 1985). The Faifa Mountains are predominantly composed of intergranular syenite, biotite schist, and sericite schist, and are dissected by north-south, northwest-southeast, and east-west trending fault systems (Fairer, 1985; Alharbi et al., 2014; Fig. 3d).



**Figure 3.** Maps showing the study area. (a) Elevation map showing locations where field observations were collected for the period extending from February 26th to March 7th, 2016. (b) Slope map generated from TanDEM-X DEM. (c) NDVI map generated from Sentinel-2 data (date of acquisition: 2017-06-05). (d) Geologic map for the Faifa Mountains (after Fairer, 1985 and Alharbi et al., 2014).

5

Analysis of TRMM and GPM measurements for the period 1998 to 2016 revealed sparse precipitation over the Saudi Arabian landscape (MAP: 83 mm/year), with the exception of the Red Sea Hills in southern Saudi Arabia, which receive an MAP of 108 mm/year. A progressive increase in overall rainfall over Faifa was noted over the past six years (MAP: 2010–2016: 315



mm/year; 1998–2009: 227 mm/year) with the wettest year on record in 2016 (total annual rainfall: 450 mm). Two systems of wind regimes are responsible for the rainfall over Faifa: (1) northerly and northwesterly winter cyclonic regimes from the Mediterranean, and (2) summer monsoons from the Arabian Gulf and the Indian Ocean (Alsharhan et al., 2001).

## 2 Methods

- 5 The methodology we developed entailed two main steps. The ID curve for the Faifa Mountains was first generated to identify storms that caused landslides (temporal analysis; Sect. 2.1), and then pixel-based ID curves were constructed to identify the locations where movement is likely to occur (spatial analysis, Sect. 2.2–2.4). The latter step involved: (1) selection, calibration, and pre-processing of radar images; (2) generation of backscatter coefficient difference images as a measure of surface roughness change due to precipitation-induced landslides; and (3) development, refinement, and validation of the model to
- 10 identify pixels susceptible to movement under user-defined precipitation conditions.

Data used for the study include: (1) Temporal Google Earth imagery, (2) Sentinel-1A radar imagery; (3) TRMM and GPM; (4) field observation of landslide (debris flow and failure along fracture plane) locations; and (5) the TanDEM-X DEM. A detailed flow chart is presented in Fig. 4.

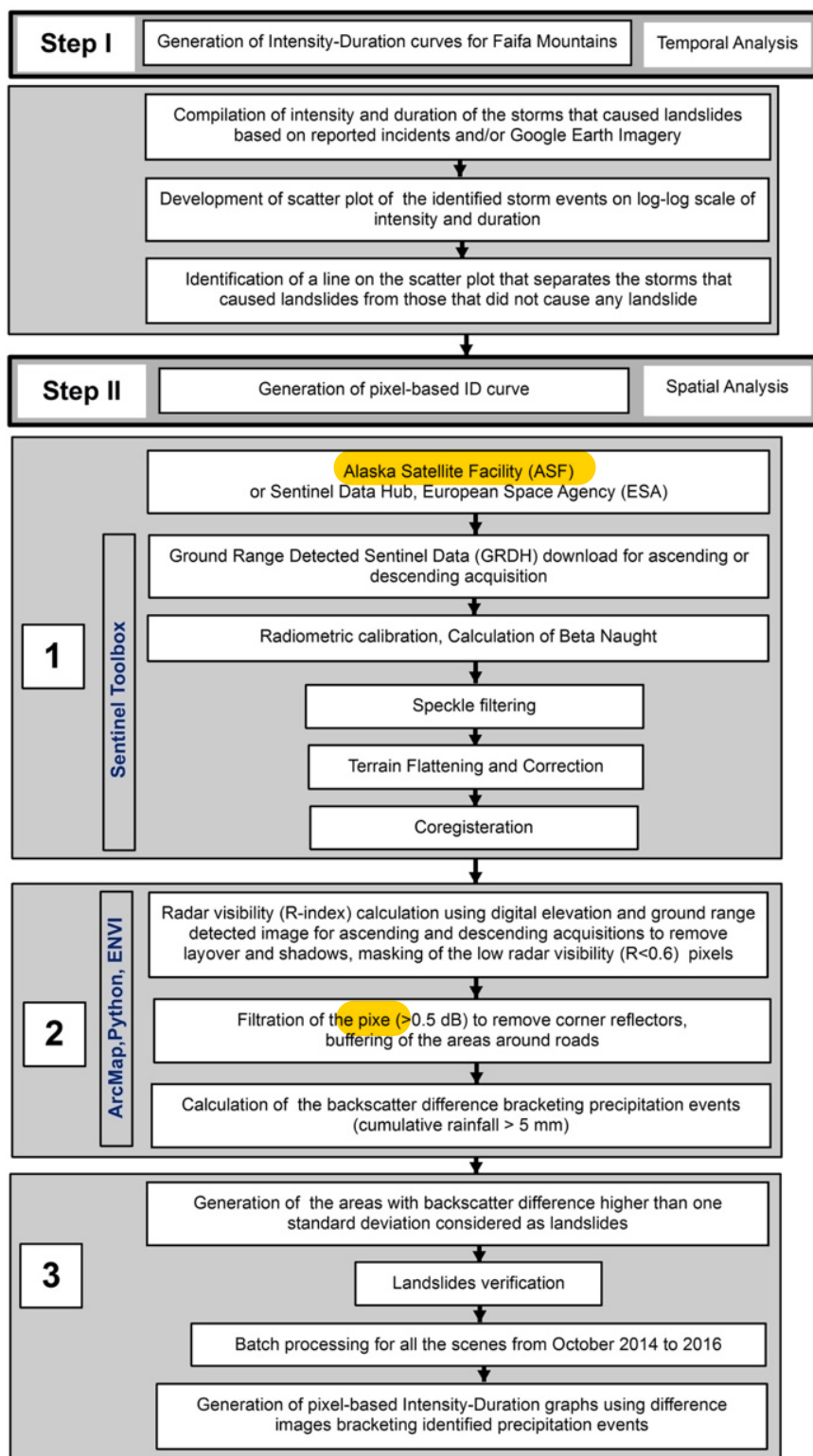




**Figure 4. Flow chart summarizing the developed methodology that could serve as important steps towards the construction of an EWSL. The developed procedures involved the analysis of temporal Google Earth images, Sentinel-1A radar scenes, and TRMM and GPM rainfall data. Analysis involved two main steps: generation of an ID curve for the Faifa Mountains to identify storms that are likely to produce landslides (landslide-producing storms), and generation of pixel-based ID curves to identify the locations where movement is likely to occur during landslide-producing storms. Step II involved: (1) selection, calibration, and pre-processing of radar images, (2) generation of backscatter coefficient difference images as a measure of surface roughness change due to precipitation-induced landslides and, (3) development, refinement, and validation of the model to identify pixels susceptible to movement under user-defined precipitation conditions. The downloaded scenes were processed using the ESA's Sentinel Toolbox software, ENVI, ArcMap, and Python.**

## 2.1 Generation of the ID curve for the Faifa Mountains

Unfortunately, the distribution of rain gauges is inadequate in the study area (Fig. 1). There is only one station within Jazan province, and three more stations in its surroundings (Fig. 1). We utilized the GPM half-hourly (spatial resolution:  $0.1^\circ \times 0.1^\circ$ ) and TRMM 3-hourly (spatial resolution:  $0.25^\circ \times 0.25^\circ$ ) data to extract the intensity and duration of rainfall that caused landslides throughout the period 2007 to 2016 (Table 1 and Fig. 5). Rainfall events of less than 1 mm/h were omitted given that no landslides were reported from the area at these low rainfall rates and TRMM could mistakenly identify fog for low rainfall events ( $<1$  mm/h; Milewski et al., 2009). Because of these reasons, the threshold of 1 mm/h was established for the precipitation data to develop the ID curve. Altogether, 131 precipitation events were extracted from TRMM and GPM data throughout this period, of which 19 events were identified as landslide-producing storms (Table 1). These storms were identified using spectral and morphologic variations associated with landslide development, variations detected in the field and/or extracted visually from pairs of Google Earth images bracketing large precipitation events. Google Earth images were favored over other readily available visible near-infrared (VNIR) satellite data sets given their high spatial resolution (15 m to 15 cm) and long temporal coverage for the study area (2007 to present). An area that witnessed landslides will be covered by spectrally dark vegetation on the Google Earth image preceding the landslide and by spectrally bright rocks and sediments on the image acquired after the landslide development. In many cases the latter image, not the former image, shows a major scar in the source area (onset of landslide) that gives way to more linear scars in vegetation along the landslide path. It is worth noting that different parts of the Faifa Mountains have differing numbers of Google Earth image acquisitions, amount of coverages, and resolutions.

Starting in October 2014, the SGS initiated a program to field-verify reports of landslide occurrences. Field observations were conducted by our research team following the December 25th, 2015 landslide-producing storm and by the SGS researchers throughout the period from October 2014 to October 2016. Our collective field investigations revealed extensive landslides following the events on December 25, 2015, April 13, 2016, April 29, 2016, August 1, 2016, and August 25, 2016 events. During a number of these storms, landslides were reported from the mountainous areas proximal to, but outside of, the study area (e.g., Youssef et al., 2014).



Using detected storm-induced spectral and morphologic variations in pairs of archival temporal Google Earth imagery, two additional landslide-producing events (November 18 and December 1, 2014) were extracted; these were apparently not reported to, or verified by, the SGS researchers during their field campaign due to their location in inaccessible areas. Using the same techniques (storm-induced spectral and morphologic variations) 16 storms were detected in the period (2007 through 2014) preceding the SGS field campaign (2014–2016). Given the paucity of Google Earth images (18 images in 10 years), a number of precipitation events are likely to have occurred between consecutive Google Earth images. If landslides were detected within the period covered by the consecutive Google Earth image acquisitions, it was assumed that the largest of these storms caused the observed landslides. In doing so, a few landslide-producing storms and those that did not cause landslides were not identified. The latter type of storms were identified during the field campaign period (Table 1).

10

**Table 1. Intensity and duration of the precipitation events used for the construction of the Faifa ID curve. Landslide-producing storms were verified through field observations and by examining spectral and morphologic variations in pairs of Google Earth archival images bracketing significant storm events.**

	Intensity (mm/h)	Duration (h)	Storm Date	Landslides	Google Earth Imagery Dates
1	3.17	3.00	2007-06-02	Yes	Google Earth (2007-12-30 and 2007-03-01)
2	4.83	3.00	2008-10-11	Yes	Google Earth (2010-04-19 and 2007-12-30)
3	5.34	3.00	2008-10-24	Yes	Google Earth (2010-04-19 and 2007-12-30)
4	2.58	3.00	2010-07-29	Yes	Google Earth (2010-10-28 and 2010-05-10)
5	2.69	6.00	2010-07-11	Yes	Google Earth (2010-10-28 and 2010-05-10)
6	3.62	3.00	2010-08-25	Yes	Google Earth (2010-10-28 and 2010-05-10)
7	1.85	6.00	2011-07-31	Yes	Google Earth (2012-03-05 and 2010-10-28)
8	1.86	9.00	2011-08-27	Yes	Google Earth (2010-10-28 and 2012-03-05)
9	3.29	3.00	2011-08-28	Yes	Google Earth (2012-03-05 and 2010-10-28)
10	2.91	3.00	2012-06-21	Yes	Google Earth (2013-04-14 and 2012-03-05)
11	1.63	6.00	2013-07-22	Yes	Google Earth (2013-10-11 and 2013-04-14)
12	1.04	12.00	2014-05-18	Yes	Google Earth (2014-12-24 and 2014-01-06)
13	3.70	2.00	2014-11-18	Yes	Google Earth (2014-12-24 and 2014-05-23)
14	5.77	4.00	2014-12-01	Yes	Google Earth (2014-12-24 and 2014-10-21)
15	2.42	1.00	2015-03-22	No	Field Visit
16	4.67	0.50	2015-06-02	No	Field Visit
17	1.77	0.50	2015-06-20	No	Field Visit
18	1.37	0.50	2015-07-31	No	Field Visit





19	2.39	1.00	2015-08-25	No	Field Visit
20	3.07	1.50	2015-09-14	No	Field Visit
21	2.62	2.00	2015-11-05	No	Field Visit
22	7.91	2.00	2015-12-25	Yes	Field visit
23	2.85	0.50	2016-03-25	No	Field Visit
24	5.02	6.50	2016-04-13	Yes	Field Visit
25	4.76	1.50	2016-04-29	Yes	Field Visit
26	2.82	2.00	2016-06-02	No	Field Visit
27	1.64	1.00	2016-06-15	No	Field Visit
28	8.85	12.00	2016-08-01	Yes	Field Visit
29	6.40	3.00	2016-08-25	Yes	Field Visit
30	2.93	2.50	2016-09-30	No	Field Visit

The data presented in Table 1 were plotted to extract the ID curve for the Faifa Mountains. Landslide-producing storms (seven storms) were represented in Fig. 5 by solid circles (red and black), and the non-landslide producing storms by open circles. The solid black circles are for field-verified landslide-producing storms, and the red circles are for landslide-producing events extracted from Google Earth images. The figure shows the extracted ID curve (red line) that provides the best visual separation between the landslide-producing (solid circles above red line) and non-producing (open circles below red line) precipitation events. For comparison purposes, additional ID curves are reported from other areas; each is characterized by its unique hydrologic, geologic, climatic, and topographic settings and plotted in Fig. 5. These include Mediterranean cool climates, the shallow landslide and debris flows, wildfire-related debris flow, shallow landslides, soil slips, debris flows, and warm mountain climates, (Caine, 1980; Innes, 1983; Clarizia et al., 1996; Crosta and Frattini, 2001; Cannon and Gartner, 2005; Guzzetti et al., 2008). The closest ID curve to the Faifa Mountains curve is that of the shallow landslide. This is to be expected given that the shallow landslide curve was generated for areas with similar climatic (precipitation: Faifa 252 mm/year; shallow landslide: >200 mm/year) and topographic (slope: Faifa: 20° to 65°; shallow landslide: 25° to 40°) settings.

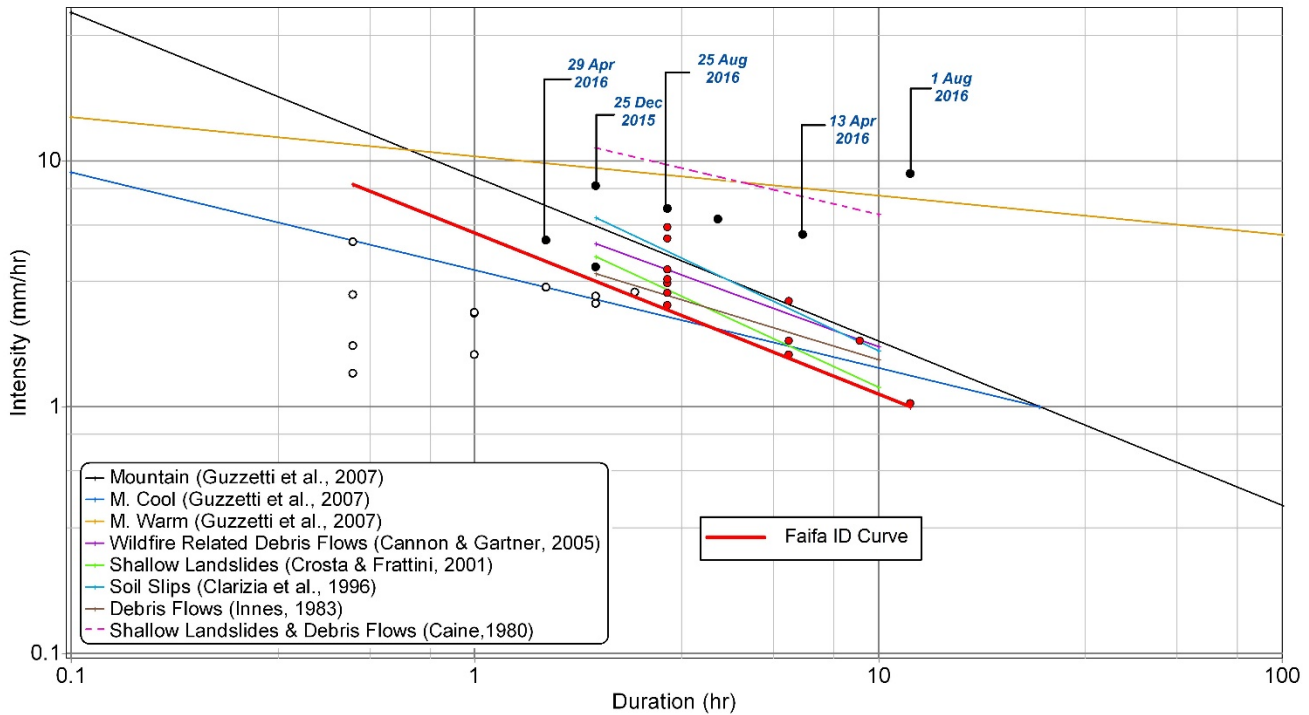


Figure 5. ID scatter plot generated from landslide-producing storm events (solid circles) and non-producing precipitation events (open circles) during the period 2007 to 2016. Faifa ID curve (equation:  $I = 4.89 \cdot D^{-0.65}$ ; duration threshold [x]: 0.5 to 12 h) separates the landslide-producing events from non-producing events. Field-verified landslide-producing storms are plotted as black solid circles and those extracted from Google Earth images as solid red circles. Also shown for comparison are published ID curves for areas with unique climatic, topographic, and geologic settings.

## 2.2 Selection, calibration, and preprocessing of radar images

The ID curve for Faifa separated the storms that caused landslides from those that did not cause any landslides. The radar backscatter differences were used to determine the location of the landslide for the storm that caused the landslides. Sentinel-1A radar scenes were downloaded for ascending and descending acquisition modes from the Sentinel Data Hub (<https://scihub.copernicus.eu/dhus/#/home>), a download platform for the European Space Agency (ESA), for the period between October 2014 and October 2016. The scene acquired immediately after (1 day or less) the rainfall were not used in the generation of backscatter coefficient difference images to avoid differences in backscatter due to precipitation-related change in moisture content. The pre-processing steps that were applied to the downloaded scenes included radiometric calibration and calculation of beta naught ( $\beta^0$ , the radar brightness coefficient), speckle filtering, terrain flattening and correction, and image co-registration. Ascending and descending scenes for the same area provide different degrees of visibility, and depending on the orientation and complexity of the topography, one acquisition mode may provide better visibility than the other.



Ground range detected (GRD) images, acquired from the Single Look Complex (SLC) were downloaded and radiometrically calibrated using ESA's Sentinel Toolbox. The GRD images were used to calculate the  $\beta^0$  (Small, 2011), a measure of radar backscatter energy in decibels (dB; Raney et al., 1994), for both ascending and descending modes. The speckle in the extracted radar backscatter coefficient images was minimized using the Lee Filter (window size:  $3 \times 3$ ; Lee, 1983; Lee et al., 2009) and high-resolution DEM (TanDEM-X DEM; resolution: 12.5 m). The Terrain Flattening and the Range Doppler Terrain Correction (Small, 2011) was applied to the speckle filtered scenes to correct for radiometric biases introduced by the rugged topography of the study area. Each of the processed scenes was co-registered (sub-pixel co-registration) to the previously acquired one in Sentinel Toolbox (Press et al., 1992).

### 2.3 Generation of backscatter difference images

The generation of the backscatter difference images involves a number of steps: (1) calculation of radar visibility, (2) removal of corner reflectors, and (3) generation of backscatter difference images.

Ascending and descending scenes for the same area provide different degrees of visibility depending on the orientation and complexity of the topography given the variations in slope, aspect, radar incidence angle, layover, and shadow (Notti et al., 2014). The radar visibility index (R; Notti et al., 2014) was used to identify and mask out areas of low visibility in both the ascending and descending scenes. The index values range from 0 (low visibility) to 1 (high visibility). Pixels with R values below a threshold of 0.6 were found to be affected by overlays and shadowing and were thus identified as low visibility areas and masked out.

The distribution of pixels with backscatter coefficients exceeding 0.5 dB were found to correlate with that of buildings, construction areas, vehicles, and parking spaces. Such features can act as corner reflectors and produce high radar returns by reflecting waves towards the source. Pixels with backscatter coefficients exceeding 0.5 dB (corner reflectors) were masked out.

The filtered backscatter images were used to generate backscatter difference images between pairs of consecutive backscatter scenes, and only those pairs bracketing storm events were considered for further analysis.

### 2.4 Refinement and validation of the model

The refinement and validation of the model involved: (1) spatial refinement and standard deviation (SD) image generation, (2) field verification, and (3) batch processing of scenes. The population density in and around the road networks is high, and so are the risks for human and property losses if landslides occur in their vicinity. The construction of roads can trigger debris flows, especially in cases when roads intersect steep slopes (Fig. 6a) or terraces constructed on these steep slopes (Fig. 6b), ephemeral valleys, and fracture planes dipping towards the road (Fig. 6c; Alharbi et al., 2014).



The distribution of historical debris flows in the study area was investigated to identify areas susceptible to debris flow. As described earlier, areas that witnessed recent debris flows are characterized by spectrally bright rocks and sediments, a major scar in the vegetation within the source area (onset of landslide) that gives way to more linear scars in the vegetation along the landslide path. As years go by, spectral and morphologic features indicative of debris flows can get obscured by encroaching  
5 vegetation making it more difficult to identify the older debris flows. Many of the historical debris flows were found on steep slopes, along first order streams, above and proximal to the main roads as shown in Fig. 5. Using these three criteria, areas susceptible to debris flows were identified by: (1) extracting stream networks using a stream delineation algorithm (Tarboton et al., 1991) in ArcGIS 10.5 over the steep slopes ( $>30^\circ$ ) and capturing first order streams, using a small flow accumulation value (10 pixels), (2) assigning a buffer zone (width: 20 m) around the extracted streams to delineate the areas that are likely  
10 to be triggered by runoff during and following rainfall events, and (3) assigning a buffer zone (width: 100 m) around the roads. The use of the latter criterion allows the identification of areas susceptible to failure along preexisting fractures as well since our field observations showed that the majority of such failures were triggered by road construction. The selected width of the buffer zones was determined by examining the proximity of the historical landslides to roads and extracted streams.

15 The selection of the buffered zones for further investigation served two purposes: (1) targeting areas of high risk, and (2) capturing the backscatter variations that are related to landslides, variations that could have been confused with those caused by factors other than landslides (e.g., change in vegetation intensity or vegetative cover) if the entire area was considered. Figure 7 shows several landslides within areas identified as being susceptible to landslides using the three above-mentioned criteria.



20

**Figure 6. Landslides proximal to, and possibly triggered by, road construction. (a) Debris flow caused by failure on steep slopes intersected by roads. (b) Debris flow caused by failure of terraces constructed on steep slopes. (c) Landslide flow caused by failure on fracture planes dipping towards the road.**

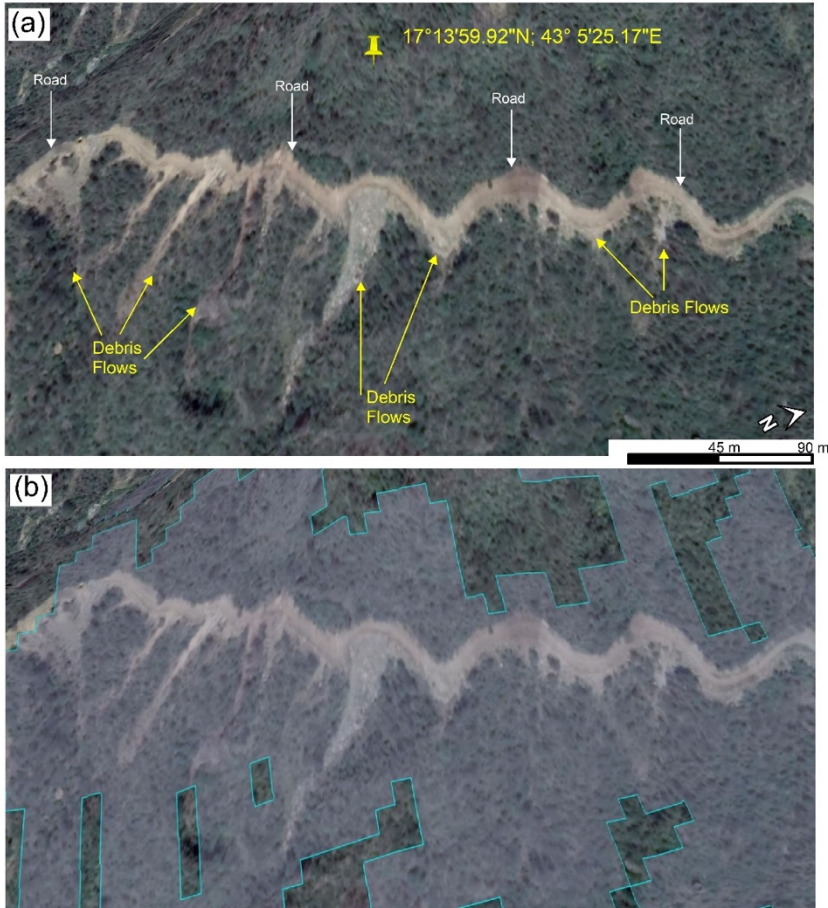


**Figure 7. Google Earth Imagery showing the spatial refinement procedures. (a) Areas showing debris flows within areas characterized by steep slopes ( $>30^\circ$ ), and proximity to roads ( $<100$  m) and to the first order streams ( $<20$  m). (b) The areas that satisfy these three conditions are outlined by the shaded polygon.**

5

The spatial refinement was followed by filtration to detect spectral anomalies in the resultant image. A standard deviation–classified image was generated for a backscatter difference image that bracketed the December event (images acquired on December 24, 2015 and February 12, 2016). The differences in backscatter were classified into four groups: area of  $\leq 1SD$  (transparent),  $>1SD$  to  $\leq 2SD$  (green),  $>2SD$  to  $\leq 3SD$  (yellow); and  $>3SD$  (red). Within the buffered areas on any of the backscatter difference images, the largest variations are expected to correspond to areas that witnessed landslide-related changes in roughness. Field observations following the December 25, 2015 precipitation event (15 mm) were conducted (February 26 to March 7, 2016) to test this assumption. The investigation proved the examination of the variations in spatially refined and spectrally filtered backscatter difference images, and the effectiveness of the applied filtering techniques in omitting the false positives.

15



Altogether we visited 27 sites in Faifa during our field investigation (Fig. 2a). It was found that the distribution of areas with  $\leq 1$ SD variations on the extracted difference images did not correspond to any of the observed landslides and are here attributed to temporal variations in vegetation, minor roughness changes, and possibly sub-pixel errors in co-registration. Areas exceeding 1SD on the difference images (Fig. 8; clusters of red, yellow, and green pixels) in the backscatter difference image corresponded to landslide locations and showed evidence for recent redistribution of boulders and sediments in the field. If these two conditions were met, a landslide was considered as being verified. Out of the 15 predicted landslides, 14 were verified in the field. There was a false positive where the pixels exceeding 1SD corresponded to road construction-related changes (Table 2: site 26). Field investigations of 12 sites verified that spatial refinement and filtration techniques was successful in filtering out 9 of the 12 false positives resulting from corner reflectors (e.g., building, constructions), but mistakenly removed an active debris (Table 2: site 1) and structurally stabilized fracture plane (Table 2: site 19 and 20).

A batch process was developed to download bi-weekly radar images (ascending and descending) and to conduct image processing tasks described in Sect. 4.2, 4.3, and 4.4. Tasks include calibration, pre-processing, generation of backscatter coefficient differences, and refinement and validation of the model. The batch process outputs include standard deviation-classified images for pairs of consecutive descending and ascending acquisitions.

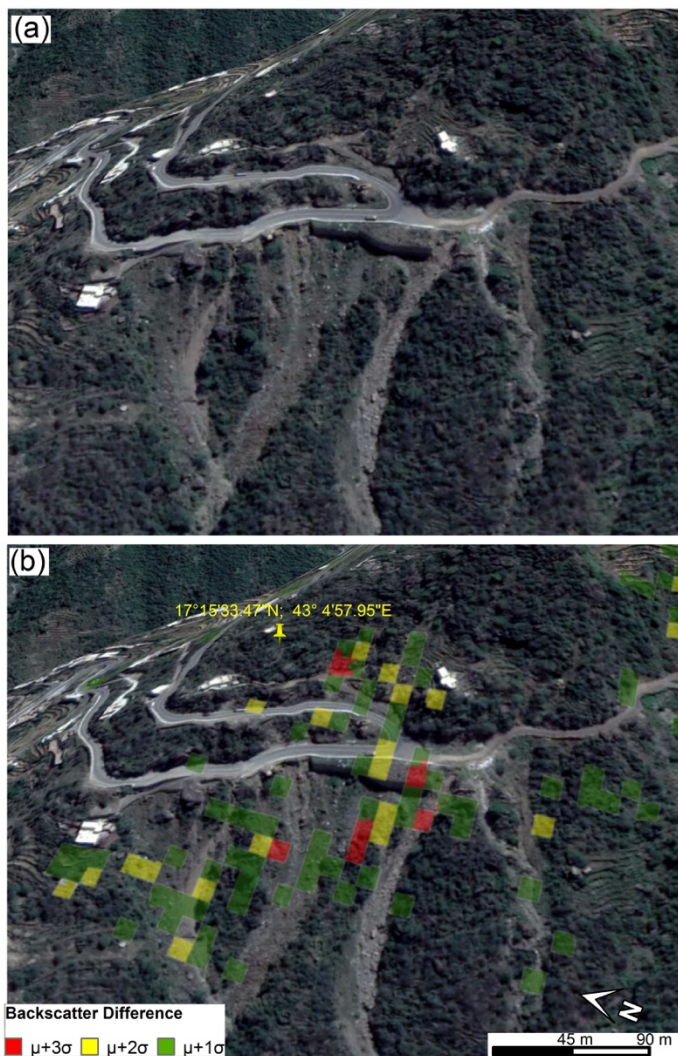


Figure 8. (a) Google Earth imagery showing the distribution of debris flows. (b) Backscatter difference image for two descending scenes bracketing (acquisition dates: December 24, 2015 and February 10, 2016) a precipitation event on December 25, 2015 showing correspondence of areas of low to negligible variations ( $\leq 1SD$ ) with vegetation and areas exceeding 1SD (clusters of red, yellow, and green pixels) to debris flow locations that showed evidence for recent redistribution of boulders and cobbles in the field.

Table 2. Field observations collected (February 26 to March 7, 2016) for the assessment of radar-based distribution of active landslides, the areas exceeding 1 standard deviation (1SD) on difference images. Locations shown in Fig. 2a.

	Difference image	Remarks	Long. (°E)	Lat. (°N)
1		<i>Filtered out active debris flow; false positive</i>	43.054	17.234
2	3SD, 2SD	Verified active debris flow	43.065	17.237
3	3SD, 2SD	Verified active debris flow	43.070	17.233



4		<i>Filtered out road construction</i>	43.080	17.236
5		<i>Filtered out terraces, bare soil, no vegetation</i>	43.081	17.237
6	3SD, 2SD	Verified active debris flow, recently mitigated at intersection with road	43.083	17.241
7	2SD	Verified active debris flow	43.086	17.244
8		<i>Filtered out terraces</i>	43.091	17.243
9	2SD	Verified active debris flow; locals reported activity during rainfall	43.092	17.244
10	2SD	Verified active debris flow used to dispose construction material	43.106	17.255
11	3SD, 2SD	Verified active debris flow, recently mitigated at intersection with road	43.105	17.262
12		<i>Filtered out buildings</i>	43.118	17.271
13	2SD	Verified active debris flow	43.118	17.273
14		<i>Filtered out road construction</i>	43.070	17.271
15		<i>Filtered out road construction</i>	43.075	17.266
16	2SD	Debris flow related to terraces	43.081	17.261
17	2SD	Verified debris flow recently mitigated proximal to road	43.081	17.262
18	3SD, 2SD	Verified active debris flow	43.081	17.260
19		<i>Filtered out shotcrete to stabilize the fracture planes; false positive</i>	43.087	17.255
20		<i>Filtered out shotcrete to stabilize the fracture planes; false positive</i>	43.086	17.258
21	3SD, 2SD	Verified active debris flow	43.082	17.258
22	2SD	Verified failure along fracture plane dipping towards the road	43.091	17.254
23		<i>Filtered out buildings</i>	43.104	17.262
24		<i>Filtered out terraces</i>	43.101	17.267
25	3SD, 2SD	Verified active debris flow bordering a terrace	43.099	17.269
26	3SD, 2SD	Construction related debris flows downhill from the road; false negative	43.095	17.273
27		<i>Filtered out construction along the road</i>	43.083	17.274

## 2.5 Pixel-based adaptation of Faifa ID curve as a predictive tool

The ID curve/line for any pixel should separate landslide-producing events (backscatter difference  $> 1SD$ ) from non-landslide producing (backscatter difference  $\leq 1SD$ ) precipitation events. On these graphs, landslide-producing events plot above the line/curve, and the non-producing events plot below it.

A pixel-based debris detection system was developed by adopting the slope of the extracted Faifa ID curve. The assignment of the ID curves to the individual pixels will depend on the relative stability of the individual pixel. The less stable pixels, such as those on steep slopes, are expected to experience movement in response to weak, moderate, and extreme storm events, whereas the more stable pixels will move during the extreme events only. Figure 9 demonstrates the ID curve for two locations:





a more stable pixel and a less stable one. The dotted line represents the ID curve for more stable locations as it showed evidence for landslide-related movement ( $>1SD$  on the radar backscatter difference image) in response to the largest storm event on August 1, 2016, and no movement ( $<1SD$  on the backscatter image) during the remaining events. The dashed line represents the ID curve for the less stable locations that showed evidence for landslide-related movement during five events (December 1, 2014, December 25, 2015, April 13, 2016, August 1, 2016, and August 25, 2016) but none following the December 25, 2016 and November 18, 2014 storms. Thus, knowing the historical response of each individual pixel to these storms, each pixel was assigned an ID curve whose slope is similar to that of the Faifa curve. In other words, the pixel-based ID curve uses the historical landslide response of a pixel to estimate the intensity and duration of the precipitation that would cause landslides in the future. Any event that plots above the pixel ID curve would produce landslides at that location, whereas the one that plots below would not produce a landslide. The pixel-based ID curve helps to predict the location that will witness landslides under any future storm event.

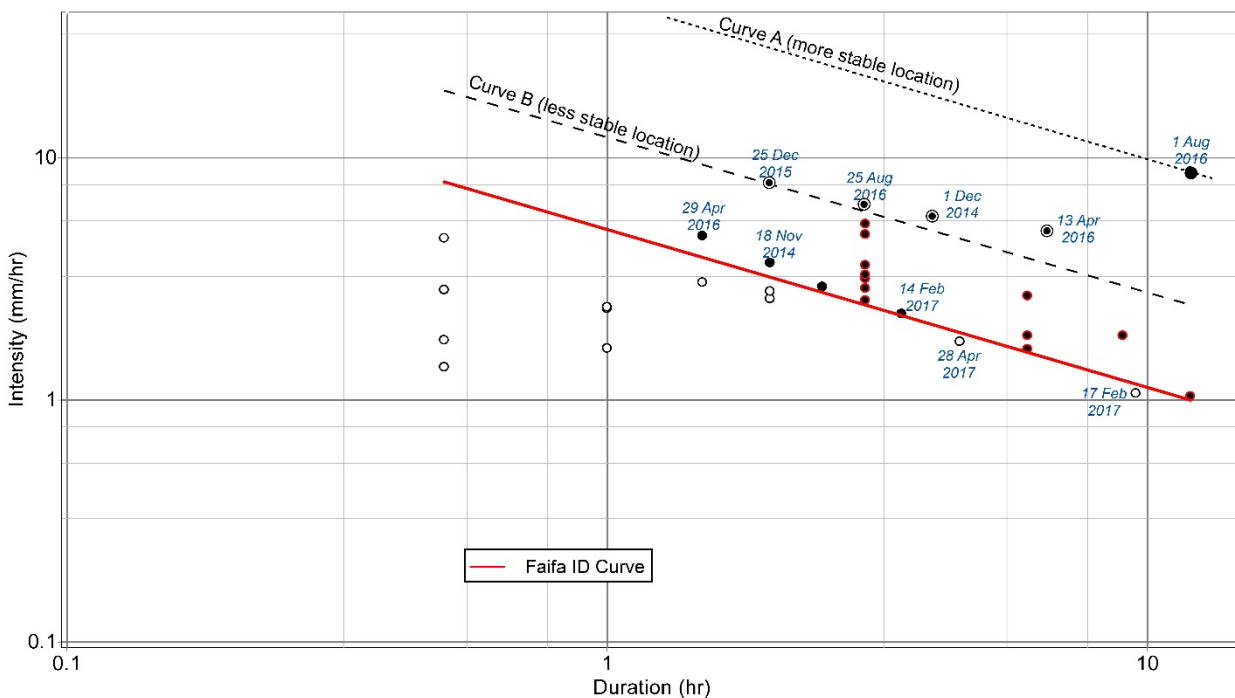


**Figure 9. Demonstration of pixel-based ID curves.** Curve “A” (dotted line) is an ID curve for a more stable pixel that witnessed landslides in response to the storm on August 1, 2016, and curve “B” (dashed line) is a curve for a less stable pixel that witnessed landslides in response to four storms (December 1, 2014, December 25, 2015, April 13, 2016, August 1, 2016, and August 25, 2016). These ID curves for stable and less stable locations are parallel to the Faifa ID curve (red line) that separates landslide-producing storm events (solid circles) from landslide non-producing storm events (open circles) from Fig. 5. The four events (solid circle within open circle) plotting between the dotted and dashed lines are landslide-producing storms (solid circle) for the less stable pixel (curve B) and non-producing storms (open circles) for the more stable pixel (curve A).

20



## 2.6 Validation of ID curve

Three precipitation events larger than the threshold (1 mm/h for 1 h) were recorded during the period from November 2016 to April 2017. These occurred on February 14 (intensity: 2.28 mm/h; duration: 3.5 h), February 17 (intensity: 1.07 mm/h; duration: 9.5 h), and April 28 (intensity: 1.75 mm/h; duration: 4.5 h) of 2017. The event on February 14 plotted above the Faifa ID curve, whereas those on February 17 and April 28 plotted below the curve. Landslides were reported following the February 14 event, but not for the two other storm events, an observation that supports the validity of the extracted ID curve for Faifa.

Using the precipitation intensity and duration for the February 14 storm, and the extracted pixel ID curves, we generated a map showing the areas (three or more pixels) that are likely to witness movement under the specified precipitation conditions. We visually inspected these areas on the Google Earth images that were acquired before (October 2, 2016) and after (March 29, 2017) the February 14 storm. Spectral and morphological variations indicative of landslides were detected on the March 29 Google Earth image. Specifically, 13 landslides were predicted, out of which 6 were verified by inspecting the March 29 image, an accuracy of 60%. This accuracy is reasonable given: (1) the uncertainties associated with extracting the Faifa and pixel-based ID curves (refer to section 4.7), and (2) the fact that landslides in a particular area tend, in some cases, to stabilize the location and reduce the chances of landslide recurrence in the same area.

## 3 Conclusions, limitations, and future work

We developed a predictive system that shows whether a storm with a particular intensity and duration can cause landslides in the Faifa Mountains. For the identified landslide-producing storms, the developed methodologies will also select areas that are likely to witness landslide development. The extracted ID curve for the Faifa is used for the former and the extracted pixel-based ID curves for the latter.

Our ability to predict the landslide-producing storms and the locations of these landslides will depend largely on the accuracy of the extracted/adopted ID curves. The production of the Faifa ID curve was based on precipitation data for 30 storms, approximately 63% of which produced landslides. Precipitation was extracted from the earlier coarse TRMM (3 h;  $0.25^\circ \times 0.25^\circ$ ) and later from the finer resolution GPM (1 h;  $0.1^\circ \times 0.1^\circ$ ) data; field observations and temporal Google Earth images were used to identify which of these storms produced landslides. The temporal coarseness of the precipitation data, especially 3-hourly TRMM data, provides the uncertainty in the precise placement of the ID curve. In upcoming years, additional data points (landslide producing and non-producing storms), especially those extracted from GPM or rain gauge data with higher spatial and temporal resolution will be used to refine the initial Faifa ID curve.

Refining the Faifa ID curve will enhance the accuracy of the pixel-based ID curves as well, given that they are assumed to be parallel to the Faifa ID curve. In the construction of these curves, we were constrained by the following limitations in data availability and processing technique: (1) the limited number of storms (18) that occurred throughout the time period (October



- 30, 2014 to October 31, 2016) during which radar images were available; (2) coarse spatial resolution of the DEM (12.5 m TanDEM-X) and radar data (multi-looked using DEM, 12.5 m) that made it difficult to identify landslides of limited distribution (<25 m); (3) the discontinuous acquisition of Sentinel-1A data (ascending and descending modes) that interrupted the monitoring of landslides in response to storm events; (4) sub-pixel errors in co-registration of radar data and anomalous  
5 backscatter spikes originating from buildings and construction activities that produced radar responses similar to landslide-related radar response and were not filtered; (5) drastic changes in the slope and/or vegetation in a particular pixel that impaired the functionality of several pixel-based ID curves; and (6) frequent rainfall with short duration could have gone undetected given the coarse temporal resolution of the satellite-based precipitation data.
- 10 In coming years, the pixel-based ID curves we developed will be refined by: (1) acquiring high spatial and temporal resolution precipitation data, (2) identifying additional landslide-producing storms to augment the existing database and update the existing pixel-based ID curves, (3) applying additional filtration techniques (e.g., coherence threshold filters to reduce false positives), and (4) developing an urban mask to exclude radar responses from corner reflectors that could be confused with those from landslides. We will also explore refining our methodologies to account for the impact of antecedent precipitation  
15 on landslide development (e.g., Chen et al., 2015). To date, the application of ID thresholds for landslide hazard assessment is widespread in early warning systems at local and regional scales (e.g., Peruccacci et al., 2017; Rossi et al., 2017), yet over the past few years there has been increasing recognition of the role of hydrology in landslide initiation, a factor that is not fully incorporated in the ID threshold analysis. The intensity and duration of rainfall during which a landslide occurs are not the only triggers for landslides; the rainfall events (antecedent rainfall) that preceded the landslide-causing precipitation are  
20 triggers, as well (Kim et al., 2014, Hong et al., 2017). It has been shown that the antecedent and peak rainfall play important role in triggering landslides in general, but debris flow development is more related to rainfall peak than antecedent rainfall (Chen et al., 2015). Given that the overwhelming majority of our landslides are debris flows, we do not anticipate that such refinement will largely affect our findings.
- 25 The adopted methodologies and the suggested refinements could eventually be used to develop an EWSL. To achieve this goal, the following additional automated steps have to be accomplished. Near real-time measurements of precipitation should be collected from the rain gauge network over the study area to avoid the delays associated with posting satellite-based precipitation (GPM: 3 to 6 hours). Temporal precipitation distributions can be derived from the acquired rain gauge measurements and used as inputs to our developed modules. Currently, our methodology identifies vulnerable areas based on  
30 user-defined precipitation intensity and duration. Once the EWSL is established, as rainfall data is collected, it will be fed automatically into the EWSL to identify the areas likely to witness landslide movement at any time. For the system to function as an early warning, the precipitation at any location could be assumed to continue for a pre-determined time period (e.g., 1 hour) and the model outputs under such assumptions could be used to predict the areas that are likely to witness landslides in that pre-determined time period. The predictive model outputs could be posted in near-real time on a web-based GIS, giving  
35 the authorities and citizens in threatened areas enough time to vacate these locations.



The methodologies advanced here are robust and cost-effective procedures that could be readily applied to many data-deficient locations worldwide. The proposed methodology relies heavily on readily available satellite data and thus could be applicable to many of the world's mountainous locations. They should not be considered as alternatives to existing field-based ID relationships, but a substitute until such datasets are acquired.

**Author Contributions:** Sita Karki processed the remote sensing data and prepared the manuscript. Mohamed Sultan supervised the project and helped in the manuscript development. Saleh A. Al-Sefry and Hassan M. Alharbi led the field investigation and data collection. Mustafa Kemal Emil and Racha Elkadiri Racha helped in the radar data processing and statistical analysis. Emad Abu Alfadail provided geographical information system technical support for the project.

**Competing interests:** The authors declare that they have no conflict of interest.

**Acknowledgements:** We would like to thank the Saudi Geological Survey for their scientific, financial, and logistical support for this project. We also acknowledge the European Space Agency for Sentinel-1A data and German Aerospace Center (DLR) for TanDEM-X data used in this study.

## References

- Alharbi, T., Sultan, M., Alsefry, S., Elkadiri, R., Ahmed, M., Chase, R., Milewski, A., Abu Abdullah, M., Emil, M., and Chounaird, K.: An assessment of landslide distribution in the Faifa area, Saudi Arabia, using remote sensing and GIS techniques, *Nat. Hazards Earth Syst. Sci.*, 14, 1553–1564, <https://doi.org/10.5194/nhess-14-1553-2014>, 2014.
- Alsharhan, A. S., Rizk, Z. A., Nairn, A. E. M., Bakhit, D. W., and Alhajari, S. A.: *Hydrogeology of an arid region: the Arabian Gulf and adjoining areas*, Elsevier, Amsterdam, Netherlands, 2001.
- Caine, N.: The rainfall intensity-duration control of shallow landslides and debris flows, *Geografiska Annaler*, 62, 23–27, <https://doi.org/10.2307/520449>, 1980.
- Cannon, S. H., and Gartner, J. E.: Wildfire-related debris flow from a hazards perspective, in: *Debris flow hazards and related phenomena*, edited by: Jakob, M., and Hungr, O., Springer, Berlin, 363–385, [http://dx.doi.org/10.1007/3-540-27129-5\\_15](http://dx.doi.org/10.1007/3-540-27129-5_15), 2005.
- Chen, C. W., Saito, H., and Oguchi, T.: Rainfall intensity–duration conditions for mass movements in Taiwan, *Prog. in Earth and Planet. Sci.*, 2, <https://doi.org/10.1186/s40645-015-0049-2>, 2015.
- Clarizia, M., Gullà, G., and Sorbino, G.: Sui meccanismi di innesco dei soil slip, in: *International conference Prevention of hydrogeological hazards: the role of scientific research*, 1, 585–597 (in Italian), 1996.



- Crosta, G. B., and Frattini, P.: Rainfall thresholds for triggering soil slips and debris flow, in: Mediterranean storms, edited by: Mugnai, A., Guzzetti, F., and Roth, G., Proceedings of the 2nd EGS Plinius Conference on Mediterranean Storms, Siena, Italy, 463–487, 2001.
- Fairer, G. M.: Explanatory notes to the geologic map of the Wadi Baysh Quadrangle, Deputy Ministry for Mineral Resources, Ministry of Petroleum and Mineral Resources, Kingdom of Saudi Arabia, Denver, Colorado, USA, 1–23, 1985.
- Greenwood, W. R., Stoesser, D. B., Fleck, R. J., and Stacey J. S.: Late Proterozoic island-arc complexes and tectonic belts in the southern part of the Arabian shield Kingdom of Saudi Arabia, US Geol. Surv. Open File Rep., 1983.
- Guzzetti, F., Peruccacci, S., Rossi, M., and Stark, C. P.: The rainfall intensity-duration control of shallow landslides and debris flows: an update, *Landslides*, 5, 3–17, <https://doi.org/10.1007/s10346-007-0112-1>, 2008.
- 10 Hong, M., Kim, J., and Jeong, S.: Rainfall intensity-duration thresholds for landslide prediction in South Korea by considering the effects of antecedent rainfall, *Landslides*, 15, 523–534, <https://doi.org/10.1007/s10346-017-0892-x>, 2017.
- Innes, J. L.: Debris flows, *Prog. Phys. Geogr.*, 7, 469–501, <https://doi.org/10.1177/030913338300700401>, 1983.
- Iverson, R.M.: The physics of debris flows, *Rev. Geophys.*, 35, 245–296, <https://doi.org/10.1029/97RG00426>, 1997.
- Kim, H. G., Lee, D. K., Park, C., Kil, S., Son, Y., and Park, J. H.: Evaluating landslide hazards using RCP 4.5 and 8.5 scenarios, *Environ. Earth Sci.*, 73, 1385–1400, <https://doi.org/10.1007/s12665-014-3775-7>, 2014.
- 15 Lee, J. S.: Digital image smoothing and the sigma filter, *Comput. Vis. Graph. Image Process.*, 24, 255–269, [https://doi.org/10.1016/0734-189X\(83\)90047-6](https://doi.org/10.1016/0734-189X(83)90047-6), 1983.
- Lee, J. S., Wen, J. H., Ainsworth, T. L., Chen, K. S., and Chen, A. J.: Improved sigma filter for speckle filtering of SAR imagery, *IEEE Trans. Geosci. Remote Sens.* 47, <https://doi.org/10.1109/TGRS.2008.2002881>, 2009.
- 20 Lowell, S.: The K M Mountain landslide near Skamokawa, *Washington Geologic Newsletter* 18:3–7, 1990.
- Mashat, A., and Basset, H. A.: Analysis of rainfall over Saudi Arabia, *Met. Env. & Arid Land Agric. Sci.*, 22, 5959–78, 2011.
- Milewski, A., Sultan, M., Jayaprakash, S. M., Balekai, R., and Becker, R.: RESDEM, a tool for integrating temporal remote sensing data for use in hydrogeologic investigations, *Comput. Geosci.*, 35, 2001–2010, <https://doi.org/10.1016/j.cageo.2009.02.010>, 2009.
- 25 Ministry of Municipal and Rural Affairs (MMRA), Faifa Municipality. <https://momra.gov.sa/>, last access: 16 August 2017.
- Norrish, N. I., and Wyllie, D. C.: Rock slope stability analysis, in: *Landslides: investigation and mitigation*, Special Report 247, edited by: Turner, A. K., and Schuster, R. L., Transportation Research Board, Board, Washington D.C., 391–425, 1996.
- Notti, D., Herrera, G., Bianchini, S., Meisina, C., García-Davalillo, J. C., and Zucca, F.: A methodology for improving landslide PSI data analysis, *Int. J. Remote Sens.*, 35, 2186–2214, 2014.
- 30 Peruccacci, S., Brunetti, M. T., Gariano, S. L., Melillo, M., Rossi, M., and Guzzetti, F.: Rainfall thresholds for possible landslide occurrence in Italy, *Geomorphology*, 290, 39–57, <https://doi.org/10.1016/j.geomorph.2017.03.031>, 2017.
- Press, W. H., Teukolsky, S. A., Vetterling, W. T., and Flannery, B. P.: *The art of scientific computing. Numerical Recipes in C*, 2nd edn., Cambridge University Press, Cambridge, United Kingdom, 1992.



- Raney, K., Freeman, A., Hawkins, B., and Bamler, R.: A plea for radar brightness, in: Proc. IEEE Geosci. Remote Sensing Symposium, Pasadena, California, 1090–1092, 1994.
- Rossi, M., Kirschbaum, D., Valigi, D., Mondini, A. C., and Guzzetti, F.: Comparison of satellite rainfall estimates and rain gauge measurements in Italy, and impact on landslide modeling. *Climate*, 5, 90, <https://doi.org/10.3390/cli5040090>, 2017.
- 5
- Small, D.: Flattening gamma: radiometric terrain correction for SAR imagery, *IEEE Trans. Geosci. Remote Sens.*, 49, 3081–3093, <https://doi.org/10.1109/TGRS.2011.2120616>, 2011.
- Stoeser, D. B., and Camp, V. E.: Pan-African microplate accretion of the Arabian shield, *Geol. Soc. Am. Bull.*, 96, 817–826, [https://doi.org/10.1130/0016-7606\(1985\)96%3C817:PMAOTA%3E2.0.CO;2](https://doi.org/10.1130/0016-7606(1985)96%3C817:PMAOTA%3E2.0.CO;2), 1985.
- 10
- Tarboton, D. G., Bras, R. L., and Rodriguez-Iturbe, I.: On the Extraction of Channel Networks from Digital Elevation Data, *Hydrol. Process.*, 5, 81–100, <https://doi.org/10.1002/hyp.3360050107>, 1991.
- Youssef A. M., Al-kathery, M., Pradhan, B., and El-sahly, T.: Debris flow impact assessment along the Al-Raith Road, Kingdom of Saudi Arabia, using remote sensing data and field investigations. *Geomat. Nat. Haz. Risk*, 1–19, <https://doi.org/10.1080/19475705.2014.933130>, 2014.

15